Mechanical Response of the Negative Electrode in Structural Batteries with Nonuniform Microstructure

Downloaded from: https://research.chalmers.se, 2026-09-09 13:22 UTC

Citation for the original published paper (version of record):

Larsson, C., Tareja, R., Larsson, F. et al (2026). Mechanical Response of the Negative Electrode in Structural Batteries with Nonuniform
Microstructure. Composites Science and Technology, 284.
http://dx.doi.org/10.1016/j.compscitech.2026.111760

N.B. When citing this work, cite the original published paper.

research.chalmers.se offers the possibility of retrieving research publications produced at Chalmers University of Technology. It covers all kind of research output: articles, dissertations, conference papers, reports etc. since 2004. research.chalmers.se is administrated and maintained by Chalmers Library

(article starts on next page)

Composites Science and Technology 284 (2026) 111760

Contents lists available at ScienceDirect

Composites Science and Technology

journal homepage: www.elsevier.com/locate/compscitech

Mechanical response of the negative electrode in structural batteries with nonuniform microstructure

Carl Larsson [a], Ramesh Talreja [b], Fredrik Larsson [a], Richa Chaudhary [a], Amanda Persdotter [a], Leif E. Asp [a,*]

[a] Department of Mechanical Engineering, Chalmers University of Technology, Gothenburg, SE-412 96, Sweden
[b] Department of Aerospace Engineering, Texas A&M University, College Station, TX-77843, USA

ARTICLE INFO

Keywords:
Computational mechanics
Representative volume element (RVE)
Porous media
Multifunctional composites
Micromechanics

ABSTRACT

A proposed structural (negative) electrode consists of carbon fibres embedded in a Structural Battery Electrolyte (SBE). The carbon fibers swell during lithiation, causing internal stresses in the composite. Geometrical features such as e.g. interfibre distance affect the resulting stresses in the SBE. For proper functioning of the structural battery, it is important to ascertain that the compressive stresses generated in the SBE do not result in material degradation. This study investigates how the nonuniform distribution of fibres inevitably caused by the battery manufacturing process affects the local stress field variations in the SBE matrix. For this, Scanning Electron Microscopy (SEM) images of the processed battery composite are produced and are used to calculate statistics of interfibre distances. A procedure for reconstruction of statistically equivalent Representative Volume Elements (RVEs) is developed and the generated RVEs are analysed in a boundary value problem with specified chemical expansion of fibres and a recently developed constitutive model for the SBE matrix. The calculated extremes in the local compressive stress show approximately 25% higher values than those in an idealized reference model with a uniform (hexagonal) fibre pattern. The importance of considering manufacturing induced nonuniform microstructure in structural batteries is thus demonstrated.

1. Introduction

The demand for high-performance energy storage systems has led to the development of multifunctional structural batteries, which provide a way to reduce structural weight in applications such as electric vehicles and aircrafts by using the load-bearing structure itself as a battery. Unlike traditional lithium-ion systems, structural batteries utilize carbon fibres both as reinforcing phase and active anode material. The fibres are embedded within a structural battery electrolyte (SBE) that provides both ionic conductivity and mechanical stiffness [1–5]. During the charging and discharging cycles, the insertion of lithium ions into the carbon fibres induces a significant chemical expansion. Because the fibres are constrained by the surrounding solid-state SBE matrix, this expansion generates complex internal stress fields that can lead to mechanical degradation or affect the electrochemical performance. Understanding these localized interactions is critical for the design of durable and efficient structural electrodes and is the aim of this study. The local interactions resulting in the generation of internal stress fields would depend on the inter-fibre distances which reduce due to the chemical expansion of fibres. The initial inter-fibre distances before the chemical expansion occurs vary spatially caused by perturbation of fibre-placement during the manufacturing process. A recent structural battery composites design has a laminated multi-cell architecture [6]. Here, a single battery cell uses a lithium iron phosphate (LFP)-coated aluminum foil as the positive electrode and carbon fibres as negative electrode. The two electrodes are separated by a glass fibre fabric separator, and the stack is impregnated by SBE. The cell manufacturing process has advanced from the earlier manual procedure to the current vacuum-infusion technique for SBE impregnation. The resulting composite lamina has unidirectional carbon fibres and SBE matrix. The structural battery manufacturing process inevitably results in disorder of the fibre distribution in the lamina cross-section. A repeating unit cell for stress analysis is therefore inadequate. Instead, in this work, we use the concept of representative volume element (RVE) developed for heterogeneous materials. We use SEM images of a structural battery composite cross-section to generate inter-fibre distance statistics. We then use these statistics to simulate virtual RVE samples in which the fibres are given a specified level of chemical expansion. In these simulations, we use for the SBE matrix the recently developed poro-visco-hyperelastic model and determine the local stress fields by numerically solving the boundary value problem on the RVE [7]. For

* Corresponding author.
E-mail addresses: calar@chalmers.se (C. Larsson), leif.asp@chalmers.se (L.E. Asp).

https://doi.org/10.1016/j.compscitech.2026.111760
Received 29 April 2026; Received in revised form 22 June 2026; Accepted 30 June 2026
Available online 10 July 2026
0266-3538/© 2026 The Authors. Published by Elsevier Ltd. This is an open access article under the CC BY license (http://creativecommons.org/licenses/by/4.0/).

the carbon fibres, we utilize a finite deformation model that incorporates lithium induced expansion and stiffness variation based on measurements [8]. The impact of disorder in the inter-fibre distances is then evaluated by examining the minimum principal (effective) stress of the computed local stress fields.

2. Experimental method and imaging

T800 polyacrylonitrile (PAN)-based carbon fibres (T800SC-12K-50C, Toray Composite Materials America, Inc.) were used as the negative electrode and processed into ultrathin unidirectional (UD) tapes (15 mm width) by Oxeon AB, Sweden. For sample preparation prior to broad ion beam scanning electron microscopy (BIB-SEM), the carbon fibre tapes were cut into specimens of approximately 1×1 cm^2. The samples were then sealed using vacuum bagging and prepared via vacuum-assisted resin infusion.

The SBE was prepared with minor modifications to a reported procedure under an argon atmosphere (1 ppm H_2O, 1 ppm O_2). A 1 M liquid electrolyte was first obtained by dissolving LiTFSI in EC:PC (1:1, 50:50 wt %). This was then mixed in equal volumes with bisphenol A methacrylate (BPAMA), followed by addition of 1 wt % azobisisobutyronitrile (AIBN). The mixture was vortexed and degassed prior to infusion. The electrolyte mixture was infused into the carbon fibre via vacuum-assisted resin infusion, followed by thermal curing at 90 °C for 45 min. After curing, the vacuum bag was removed, and the resulting composite samples (carbon fibre impregnated with SBE) were collected. Prior to BIB-SEM analysis, residual liquid electrolyte phase was removed by immersing the samples in deionized water for 24 h. The samples were subsequently dried in an oven at 90 °C for 12 h.

To enable reliable microstructural characterization for subsequent RVE reconstruction, high-quality cross-sectional SEM images of the structural battery electrodes were required. Due to the mechanical fragility of the electrode and the risk of debonding of the SBE and the carbon fibres, a gentle preparation procedure was employed.

Cross sections were prepared by BIB milling using a Hitachi ArBlade system equipped with an Ar-ion gun. Prior to milling, the electrode material was pre-cut with scissors to fit the sample holder. To minimize cutting-induced debonding, the SBE was applied after pre-cutting. Excess SBE was subsequently removed by two short BIB milling steps (6 kV, ±30° swing motion, 5 min each), manually, incrementally advancing the cross-sectional edge by 100 μm per step. Final cross-sectional polishing was then performed at 6 kV for 3 h and an overhang of 100 μm, with a ±30° swing motion to reduce curtaining artefacts.

The prepared cross sections were imaged using a Zeiss Ultra 55 SEM equipped with a field-emission gun. Imaging was carried out at an accelerating voltage of 500 V and a working distance of approximately 2.3 mm. Secondary electron images were acquired using an in-lens detector at magnifications of 1000–2000× along the 1–2 mm wide BIB-milled cross-section.

3. Structural negative electrode microstructure

3.1. Preliminaries

The manufacturing process for structural battery composites of interest has been described in detail in Siraj et al. [6]. As described and outlined above, the carbon fibre electrode is impregnated with SBE using vacuum infusion. While the carbon fibres are nearly uniformly distributed before infusion, the infusion process inevitably perturbs their positions resulting in nonuniformity that cannot be described in deterministic terms due to the uncertainty of knowing the exact dynamics of the interaction between the fibres and the infused SBE. Following the approaches taken for polymer matrix composites where manufacturing processes such as autoclave curing and liquid compression moulding result in nonuniform distribution of fibres, we adopt the concept of a representative volume element (RVE) constructed to statistically represent the microstructure. In the following, we briefly summarize the main approaches for constructing RVEs and motivate the approach adopted here for the structural battery microstructure.

3.2. RVE concepts and minimum RVE size

The earliest concept of an RVE is attributed to Hill [9] who proposed that effective properties of heterogeneous reinforced solids can be expressed as averages over a volume element of a sufficiently large size. He then gave a rigorous procedure applicable to elastic solids for determining the minimum size of such an element. The procedure consists of determining the smallest volume element on the boundaries of which applying uniform traction (or displacement) produces uniform displacement (or traction). While such volume is useful for the purpose of estimating effective properties, it is not necessarily sufficient to analyse failure within the RVE. To resolve this problem, Pyrz [10] proposed to use statistical descriptors of the local disorder in the inter-fibre distances on the assumption that the local stress field within a composite was governed by these. Using descriptors of spatial point patterns derived by Ripley [11], he demonstrated that the local disorder in fibre distributions had a significant effect on the mean field quantities over a certain distance. Trias et al. [12] went further along these lines and examined the variation of the local stress and strain fields for a carbon fibre reinforced epoxy composite for different RVE sizes. Based on the coefficient of variation of the stress and strain fields, they found that the minimum required side length of a square-shaped region of the composite cross-section was 50 times the fibre radius. While no general rules for minimum RVE size appear to exist, it is prudent to use an appropriate statistical descriptor of inter-fibre distance variation along with a relevant local stress invariant to determine the adequate RVE size. This approach will be used here for the structural battery microstructure.

3.3. RVE construction procedures

Over the years numerous proposals for constructing RVEs have emerged. A recent review provides a comprehensive account of these [13]. The proposed procedures for constructing RVEs are usually described in the form of algorithms to randomly disperse fibres in a square region of composite cross-section given the fibre diameter and fibre volume fraction along with a descriptor of inter-fibre distance. The proposed algorithms differ in the type and sequence of actions taken to reach the targeted parameters avoiding fibre overlaps. The starting point in an algorithm could be a single fibre or a uniform pattern of fibres. In the former case, the RVE region is filled fibre-by-fibre in a random manner and in the latter case, a random perturbation (called shaking) is given to the selected uniform fibre pattern.

Whatever is the preferred algorithm for constructing an RVE, the important point is to have proper and adequate statistical representation of the actual composite. As noted above, the inter-fibre distance variation is assumed to be of most relevance for capturing initiation of the critical failure event. Recognizing that the inter-fibre distance variation results from the manufacturing process employed, a useful way to estimate a descriptor of this distance is from images of a composite cross-section, if available. Alternatively, the inter-fibre distance variability can be treated in a parametric manner as a degree of nonuniformity of fibre distribution. An algorithm for this purpose was developed in [14]. In the present study, SEM images of the composite cross-section were produced, as described above in Section 2. The RVE reconstruction using these images is described next.

3.4. RVE reconstruction from SEM images

As described above, the objective of the reconstruction is to generate synthetic RVEs that reproduce the spatial correlation of the observed fibre centroids from rectangular SEM images of the cross-section, shown in Fig. 1. We shall assume that the SEM images as well as the RVEs are periodic in the horizontal direction associated with the basis vector $\boldsymbol{e}_2$. The basis $\boldsymbol{e}_3$ is associated with the vertical direction and $\boldsymbol{e}_1$ in the axial direction of the carbon fibres. In total, ten unique manually segmented

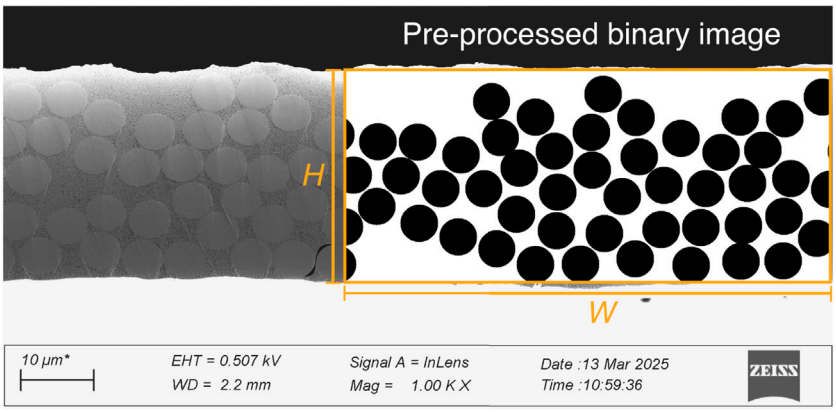

Fig. 1. SEM image of the structural negative electrode cross-section, as well as a manually segmented representation of the SEM image of width W and height H.

SEM images are considered for the analysis. The individual SEM images vary in width, height and fibre volume fraction as presented in Table 2 in the Results section. For the subsequent reconstruction steps, we shall only consider the observed mean image height and fibre volume fraction, whereas the effect of the width and spatial arrangement of fibres will be further analysed.

To quantify the spatial arrangement of fibre centroids, we employ Ripley's K-function [11] defined as

$$K(r) := \frac{1}{\lambda}\mathbb{E}\left[\text{number of centroids within distance } r \text{ of a typical centroid}\right], \tag{1}$$

where $\mathbb{E}[\bullet]$ is the expectation operator and $\lambda = N/A$ denotes the point intensity, i.e., the number of centroids N per unit area A. For a completely spatially random (CSR) process, the K-function becomes $K_{\text{CSR}}(r) = \pi r^2$ in an infinite two-dimensional domain. In practice, however, the K-function is determined by counting discrete carbon fibre centroids extracted from segmented SEM images inside a finite domain. This discrete K-function is denoted $\hat{K}(r)$. By comparing $\hat{K}(r)$ to the complete spatial randomness (CSR) benchmark, the morphological state of the electrode can be categorized. Values of $\hat{K}(r) < K_{\text{CSR}}(r)$ indicate spatial dispersion, whereas $\hat{K}(r) > K_{\text{CSR}}(r)$ represents clustering of points.

In this work, we modify the discrete Ripley's K-function tailored to the geometry of the SEM images and assumed horizontal periodicity. The source SEM images in this study are high-aspect-ratio rectangles where the width significantly exceeds the height. In such elongated geometries, any sufficiently large search disc B_r will frequently intersect the vertical boundaries of the observation window. Standard edge-correction methods (cf. Goreaud and Pélissier [15]) treat these boundaries as information loss zones, which can lead to numerical instability at large search radii or fail to capture the physics of the underlying microstructure. To maintain consistency with horizontal periodicity, we treat the SEM image and RVE reconstruction centroid patterns as infinite periodic strips.

Let the observation window have width W and height H (see Fig. 1). The original set of N centroids $\{\boldsymbol{x}_i\}_{i=1}^{N}$ is replicated periodically along the horizontal direction so that

$$\boldsymbol{x}_j^{(k)} = (x_j + kW, y_j), \quad k \in \mathbb{Z}, \tag{2}$$

where k denotes a horizontal translation index and $\mathbb{Z}$ is the set of integers. The pairwise distance between a reference centroid i and a translated neighbour j is then defined as

$$d_{ij}^{(k)} = \sqrt{(x_i - x_j - kW)^2 + (y_i - y_j)^2}. \tag{3}$$

In practice, the infinite sum is truncated to a finite range $k \in [-n_{\text{tiles}}, n_{\text{tiles}}]$, where $n_{\text{tiles}} = \lceil r_{\max}/W \rceil$ ensures that all neighbouring centroids within the maximum evaluation radius $r_{\max}$ are accounted for. By summing the contributions of all periodic neighbours within the truncated range, we arrive at the estimator for the periodic strip K-function

$$\hat{K}(r) = \frac{1}{\lambda N}\sum_{i=1}^{N}\sum_{j=1}^{N}\sum_{k=-n_{\text{tiles}}}^{n_{\text{tiles}}} \mathbf{1}\left(d_{ij}^{(k)} \le r\right), \quad \text{where } i \neq j \text{ for } k = 0. \tag{4}$$

In this formulation, $\lambda = N/(WH)$ represents the average intensity and the indicator function $\mathbf{1}(\bullet)$ identifies all pairs within the search radius r across the tiled domains.

Under the assumption of horizontal periodicity and vertical boundedness, the appropriate reference for complete spatial randomness corresponds to a homogeneous Poisson process within an infinite strip of height H. The CSR expectation, $K_{\text{CSR}}(r)$, is defined as the mean accessible area of a circle B_r of radius r, centred at a uniformly distributed height $y \in [0, H]$ within the strip. This is expressed as

$$K_{\text{CSR}}(r) = \frac{1}{H}\int_0^H \left|B_r(r, y) \cap \mathcal{B}\right| \mathrm{d}y, \tag{5}$$

where $\mathcal{B} = [-\infty, \infty] \times [0, H]$ denotes the infinite strip domain.

To identify the relevant range of spatial correlations, we employ the pair correlation function defined as

$$g(r) = \frac{\mathrm{d}\hat{K}(r)/\mathrm{d}r}{\mathrm{d}K_{\text{CSR}}(r)/\mathrm{d}r}. \tag{6}$$

As r increases, spatial correlations typically decay until the point pattern behaves as a random process, indicated by $g(r) \to 1$. We utilize this property to define the maximum evaluation radius, $r_{\max}$, as the distance at which $g(r)$ first converges to unity. By evaluating the pair correlation function using the periodic estimator in Eq. (4) and the infinite strip corrected baseline in Eq. (5), we ensure that the high-aspect-ratio geometry of the SEM windows does not introduce vertical boundary bias.

3.5. Reconstruction algorithm

In order to initialize the reconstruction procedure, an initial centroid configuration $\boldsymbol{X}_0 \in \mathbb{R}^{(n_{\text{fibres}} \times 2)}$ is generated by placing n_{fibres} points on a hexagonal lattice. This arrangement provides a uniform starting configuration while satisfying the geometric constraints imposed on the reconstruction problem. In particular, the initialization enforces (i) a minimum fibre–fibre separation distance, (ii) non-intersection of fibres with the horizontal boundaries of the domain, and (iii) periodicity in the horizontal direction. The total number of fibres is determined from the mean fibre volume fraction measured from the SEM images assuming circular fibre cross sections of a constant radius r_{f}. We base this assumption on the results by Gusev et al. [16] who found that

a variation in radius does not have a significant effect on the RVE transverse elastic properties. The number of fibres in a reconstruction domain of width W and height H is estimated as

$$n_{\text{fibres}} = \frac{\mu W H}{\pi r_{\text{f}}^2}, \tag{7}$$

rounded to the nearest integer. To ensure that the initial configuration satisfies the non-overlap constraint, a minimum centre-to-centre separation distance $d_{\min} = 2r_{\text{f}} + h$ is prescribed between neighbouring fibres, where h is a prescribed clearance distance. The hexagonal lattice spacing is then chosen so that this minimum separation is respected throughout the domain. The reconstruction problem is formulated as an optimization task to minimize the discrepancy between the reconstructed and experimental spatial statistics where the loss function is defined as

$$L = \sum_r \frac{1}{r^2} \left[\hat{K}(r) - \langle \hat{\boldsymbol{K}}_{\text{observed}}(r) \rangle\right]^2. \tag{8}$$

$\hat{\boldsymbol{K}}_{\text{observed}}(r)$ denotes the collection of vectors of the estimated K-functions from the ten SEM images, and $\langle \hat{\boldsymbol{K}}_{\text{observed}}(r) \rangle$ denotes the corresponding mean K-function. This mean serves as the primary target for the reconstruction, while the full range of experimental observations defines the acceptable variability band used for final validation. To minimize this loss, a simulated annealing algorithm is employed, as summarized in Algorithm 1 [17]. The process begins with an initial configuration that is iteratively refined; at each step, a fibre centroid is randomly selected and perturbed by a small stochastic displacement. These moves are accepted or rejected based on a Metropolis criterion governed by the change in the loss function L and a decreasing temperature parameter T [18]. The optimization proceeds until the reconstructed spatial structure sufficiently matches the experimental spread. Specifically, a candidate centroid set $\boldsymbol{X}$ is accepted as an adequate representative RVE if 98 % of the points in its estimated $\hat{K}(r)$ curve lie within the observed min.-max. variability band of $\hat{\boldsymbol{K}}_{\text{observed}}(r)$. It should be recognized further that the reconstruction relies solely on second-order statistics, meaning that smaller domain windows inherently introduce higher statistical uncertainty when capturing localized fibre clusters. Consequently, representativeness for local stress extremes is achieved asymptotically by scaling the domain width W.

Algorithm 1 Simulated Annealing for K-function Matching

Require: Target function $\langle \hat{\boldsymbol{K}}_{\text{observed}}(r) \rangle$, initial centroids $\boldsymbol{X}_0 = \{\boldsymbol{x}_0, \boldsymbol{x}_1, \ldots, \boldsymbol{x}_{n_{\text{fibres}}}\}$
Require: Step size σ, cooling rate α, initial temperature T_0
$\boldsymbol{X} \leftarrow \boldsymbol{X}_0$
$T \leftarrow T_0$
Compute initial loss
$L = \sum_r \frac{1}{r^2} \left[\hat{K}(\boldsymbol{X}; r) - \langle \hat{\boldsymbol{K}}_{\text{observed}}(r) \rangle\right]^2$
for $k = 1$ to N_{iter} **do**
  Randomly select fibre index i
  Draw displacement $\Delta\boldsymbol{x} \sim \mathcal{N}(0, \sigma^2 \boldsymbol{I})$
  $\boldsymbol{x}_i' \leftarrow \boldsymbol{x}_i + \Delta\boldsymbol{x}$
  Apply periodic boundary conditions in the 2 direction
  if $\boldsymbol{x}_i'$ violates geometric constraints **then**
    Reject move and proceed to next iteration
  end if
  Compute updated loss L'
  $\Delta L \leftarrow L' - L$
  if $\Delta L \leq 0$ **or** $\text{rand}(0,1) < \exp(-\Delta L/T)$ **then**
    Accept move: $\boldsymbol{X} \leftarrow \boldsymbol{X}'$
    $L \leftarrow L'$
    if $\hat{K}(r)$ lies inside experimental band **then**
      return $\boldsymbol{X}$
    end if
  end if
  $T \leftarrow \alpha T$
end for
return $\boldsymbol{X}$

4. Analysis of local stress field

The RVE domain, $\Omega_\square$, now consists of a carbon fibre domain $\Omega^{\text{f}} = \bigcup_{i=1}^{n} \Omega_i^{\text{f}}$, and a SBE domain Ω^{SBE} so that $\Omega_\square = \Omega^{\text{f}} \cup \Omega^{\text{SBE}}$. Moreover, we denote the top, bottom, left and right boundaries as $\Gamma_\square^{\text{T}}$, $\Gamma_\square^{\text{B}}$, $\Gamma_\square^{\text{L}}$ and $\Gamma_\square^{\text{R}}$, respectively. The carbon fibres are subjected to a normalized homogeneous and instantaneous lithium concentration field, $c_{\text{Li}} \in [0, 1]$, causing anisotropic expansion. Here, we note that the variable c_{Li} denotes a relative concentration, normalized by the saturation concentration of lithium in the carbon fibres. The application of the time-dependent concentration field will be the primary load-case of this study, restricted to a single rate of full lithiation in 10 h, i.e., $c_{\text{Li}} = 1$ at t=36 000 s. While transient lithium concentration gradients inevitably develop during active charging, evaluating the system at a state of uniform full lithiation ($c_{\text{Li}} = 1$) represents the steady-state scenario reached after sufficient time has elapsed for internal gradients to flatten. Since this state forces the maximum expansion across all fibres simultaneously, it can be considered a conservative, "worst-case" scenario for the mechanical response of the surrounding matrix.

To enable simulations of the carbon fibre expansion and corresponding stress analysis in the SBE matrix, we solve the linear momentum balance as well as balance of mass in the SBE domain, using finite deformation kinematics, inspired by previous work [7,8]. The goal is to simulate the microscopic stresses while the electrode is considered as macroscopically stress free. Hence, we adopt a multiscale framework where the displacement field $\boldsymbol{u}$ is decomposed into macro- and microscale parts as

$$\boldsymbol{u} = \boldsymbol{u}^{\text{M}} + \boldsymbol{u}^{\mu}. \tag{9}$$

The related deformation gradient can now be expressed as

$$\boldsymbol{F} = \boldsymbol{I} + \boldsymbol{u} \otimes \boldsymbol{\nabla}_X = \bar{\boldsymbol{F}} + \boldsymbol{H}^{\mu}, \tag{10}$$

where $\boldsymbol{H}^{\mu} = \boldsymbol{u}^{\mu} \otimes \boldsymbol{\nabla}_X$ is the microscale displacement gradient and $\boldsymbol{\nabla}_X$ is the (2D) gradient operator in reference configuration. We express the microscale displacements as $\boldsymbol{u}^{\mu} = u_2^{\mu}\boldsymbol{e}_2 + u_3^{\mu}\boldsymbol{e}_3$ and introduce macroscopic deformation gradients as $\bar{\boldsymbol{F}} = \bar{F}_{11}\boldsymbol{e}_1 \otimes \boldsymbol{e}_1 + \bar{F}_{22}\boldsymbol{e}_2 \otimes \boldsymbol{e}_2 + \bar{F}_{33}\boldsymbol{e}_3 \otimes \boldsymbol{e}_3$. Note that the macroscopic deformation gradient $\bar{\boldsymbol{F}}$ is not resolved as a field, the components $\bar{F}_{11}$ and $\bar{F}_{22}$ are determined to enforce a macroscopically stress free electrode, while $\bar{F}_{33} = 1$ is prescribed. A macroscopically stress free electrode in the 3-direction is obtained by applying appropriate boundary conditions on $\Gamma_\square^{\text{T}}$ and $\Gamma_\square^{\text{B}}$ in the boundary value problem. The variation of the microscale displacement gradient has the following form

$$\delta\boldsymbol{H}^{\mu} = \frac{\partial \delta u_2^{\mu}}{\partial X_3}\boldsymbol{e}_2 \otimes \boldsymbol{e}_3 + \frac{\partial \delta u_2^{\mu}}{\partial X_2}\boldsymbol{e}_2 \otimes \boldsymbol{e}_2 + \frac{\partial \delta u_3^{\mu}}{\partial X_2}\boldsymbol{e}_3 \otimes \boldsymbol{e}_2 + \frac{\partial \delta u_3^{\mu}}{\partial X_3}\boldsymbol{e}_3 \otimes \boldsymbol{e}_3. \tag{11}$$

Moreover, we introduce periodic boundary conditions for displacements on the left and right boundaries. Any quantity associated with the right boundary is denoted with $\bullet^+ \in \Gamma_\square^{\text{R}}$ and conversely, quantities on the left boundary are denoted $\bullet^- \in \Gamma_\square^{\text{L}}$, we introduce the jump $[\![\bullet]\!] = \bullet^+ - \bullet^-$. Hence, the mechanical boundary-value-problem can be stated as

$$-\boldsymbol{P} \cdot \boldsymbol{\nabla}_{\text{X}} = \boldsymbol{0} \quad \text{in} \quad \Omega_\square, \tag{12a}$$

$$\boldsymbol{P} \cdot \boldsymbol{N} = \boldsymbol{0} \quad \text{on} \quad \Gamma_\square^{\text{T}} \cup \Gamma_\square^{\text{B}}, \tag{12b}$$

$$[\![\boldsymbol{u}^{\mu}]\!] = \boldsymbol{0}, \quad [\![\boldsymbol{P}]\!] \cdot \boldsymbol{N}^+ = \boldsymbol{0} \quad \text{on} \quad \Gamma_\square^{\text{L}} \cup \Gamma_\square^{\text{R}}, \tag{12c}$$

where $\boldsymbol{P}$ denotes the first Piola–Kirchhoff stress and $\boldsymbol{N}$ is the outwards pointing unit normal vector. Furthermore, the porous-media problem

associated with the SBE domain is formulated as

$$\partial_t \boldsymbol{\Phi} + \left[\rho^{\mathrm{F}} \phi \boldsymbol{W}\right] \cdot \boldsymbol{\nabla}_{\mathrm{X}} = 0 \quad \text{in} \quad \Omega^{\mathrm{SBE}}, \tag{13a}$$

$$p = 0 \quad \text{on} \quad \Gamma^{\mathrm{T}}_{\square} \cup \Gamma^{\mathrm{B}}_{\square}, \tag{13b}$$

$$[\![p]\!] = 0, \quad [\![\boldsymbol{W}]\!] \cdot \boldsymbol{N}^{+} = 0 \quad \text{on} \quad \Gamma^{\mathrm{L}}_{\mathrm{SBE}} \cup \Gamma^{\mathrm{R}}_{\mathrm{SBE}}, \tag{13c}$$

$$\boldsymbol{W} \cdot \boldsymbol{N} = 0 \quad \text{on} \quad \partial\Omega^{\mathrm{f}} \cap \partial\Omega^{\mathrm{SBE}} \tag{13d}$$

where the storage function is defined as

$$\boldsymbol{\Phi} := J \phi \rho^{\mathrm{F}}. \tag{14}$$

Here, ϕ denotes the current porosity, ρ^{F} the fluid density in the SBE, and $\boldsymbol{W}$ the seepage velocity of the fluid relative to the solid skeleton. The quantity $J = \det(\boldsymbol{F})$ represents the local volume ratio. The governing equation Eq. (13a) expresses the conservation of fluid mass in the deforming porous medium, combining the rate of change of stored fluid mass with the divergence of the fluid mass flux. Since the pore pressure p is only defined in the SBE matrix and not in the fibre domain, periodic boundary conditions for the pore pressure field are imposed only on the SBE portions of the vertical boundaries, i.e., on $\Gamma^{\mathrm{A}}_{\mathrm{SBE}} = \Gamma^{\mathrm{A}}_{\square} \cup \partial\Omega_{\mathrm{SBE}}$ for A=T/B/R/L. The space–time continuous weak format of Eqs. (12) and (13) becomes:

For given concentration field $c_{\mathrm{Li}}(t)$, find $\delta\boldsymbol{u}^{\mu}(\boldsymbol{x},t) \in \mathbb{U}_{\square}$, $\delta p(\boldsymbol{x},t) \in \mathbb{P}$, $\delta\bar{F}_{11}(t) \in \mathbb{L}_2$, $\delta\bar{F}_{22}(t) \in \mathbb{L}_2$ for $t \in [0,T]$ such that

$$\int_{\Omega_{\square}} \boldsymbol{P}(c_{\mathrm{Li}}(t), \boldsymbol{F}) : \delta\boldsymbol{H}^{\mu} \mathrm{d}\Omega = 0 \qquad \forall \delta\boldsymbol{u} \in \mathbb{U}_{\square}, \tag{15a}$$

$$\delta\bar{F}_{11} \frac{1}{|\Omega_{\square}|} \int_{\Omega_{\square}} P_{11} \mathrm{d}\Omega = 0 \quad \forall \delta\bar{F}_{11} \in \mathbb{L}_2, \tag{15b}$$

$$\delta\bar{F}_{22} \frac{1}{|\Omega_{\square}|} \int_{\Omega_{\square}} P_{22} \mathrm{d}\Omega = 0 \quad \forall \delta\bar{F}_{22} \in \mathbb{L}_2, \tag{15c}$$

$$\int_{\Omega^{\mathrm{SBE}}} \partial_t \boldsymbol{\Phi} \delta p \mathrm{d}\Omega - \int_{\Omega^{\mathrm{SBE}}} \rho^{\mathrm{F}} \phi \boldsymbol{W} \cdot \left[\boldsymbol{\nabla}_{\mathrm{X}} \delta p\right] \mathrm{d}\Omega = 0 \qquad \forall \delta p \in \mathbb{P}. \tag{15d}$$

The top and bottom boundaries, $\Gamma^{\mathrm{T}}_{\square}$ and $\Gamma^{\mathrm{B}}_{\square}$ are subjected to traction-free and zero pore pressure boundary conditions in Eqs. (12b) and (13c). This choice is physically motivated by the manufacturing state of the electrode, which is evaluated prior to full stack lamination, leaving the top surface unconstrained. The bottom boundary interfaces with a separator in the final cell assembly, making the traction-free assumption an approximation on that specific face. This approach is favoured over kinematic constraints such as zero displacement, which would introduce over-confinement and introduce artificial stresses. Furthermore, the electrode is considered as macroscopically stress free through Eqs. (15b) and (15c). The mechanical and transport behaviour of the RVE is governed by the distinct constitutive responses of the carbon fibres and the SBE matrix. Given the multiphysics nature of the problem, we merely summarize the essential relations below; a more comprehensive derivation in the context of structural batteries can be found in [7,8]. The relevant material parameters for the models described in the subsequent sections are given in Table 1.

4.1. Description of the carbon fibre domain

For the fibre domain Ω^{f}, we adopt a hyperelastic model that accounts for the "free" deformation induced by lithium-ion insertion. Following standard finite strain theory, we utilize a multiplicative split of the deformation gradient

$$\boldsymbol{F} = \boldsymbol{F}^{\mathrm{e}} \cdot \boldsymbol{F}^{\mathrm{ch}}, \tag{16}$$

where the chemical deformation gradient $\boldsymbol{F}^{\mathrm{ch}}(c_{\mathrm{Li}})$ represents the anisotropic expansion of the lattice. We assume transverse isotropy relative to the longitudinal fibre axis $\boldsymbol{e}_1$ so that

$$\boldsymbol{F}^{\mathrm{ch}}(c_{\mathrm{Li}}) = \boldsymbol{I} + \boldsymbol{\alpha}^{\mathrm{ch}} c_{\mathrm{Li}}, \quad \boldsymbol{\alpha}^{\mathrm{ch}} = \alpha^{\mathrm{ch}}_{\mathrm{L}} \boldsymbol{e}_1 \otimes \boldsymbol{e}_1 + \alpha^{\mathrm{ch}}_{\mathrm{T}} \left[\boldsymbol{e}_2 \otimes \boldsymbol{e}_2 + \boldsymbol{e}_3 \otimes \boldsymbol{e}_3\right], \tag{17}$$

Table 1
Summary of material parameters for the carbon fibre reinforcement and the structural battery electrolyte (SBE).

Symbol	Description	Value	Source
Carbon fibre properties (Transversely Isotropic)			
E_{L}	Longitudinal modulus	$294(1 - 0.12c_{\mathrm{Li}})$ GPa	[19]
E_{T}	Transverse modulus	$21.8(1 + 1.07c_{\mathrm{Li}})$ GPa	[19]
ν_{TT}	Transverse Poisson's ratio	0.2	[8]
ν_{LT}	Major Poisson's ratio	0.22	[8]
G_{LT}	In-plane shear modulus	12.5 GPa	[8]
$\alpha^{\mathrm{ch}}_{\mathrm{T}}$	Chemical exp. (trans.)	0.066	[19]
$\alpha^{\mathrm{ch}}_{\mathrm{L}}$	Chemical exp. (long.)	0.0085	[20]
Structural battery electrolyte properties (Poro-hyper-viscoelastic)			
μ_1	Static shear modulus	29.0 MPa	[7]
κ_1	Static bulk modulus	63.2 MPa	[7]
μ_2	Dynamic shear modulus	55.7 MPa	[7]
t_*	Relaxation time	8.66 s	[7]
n	Norton exponent	6.18	[7]
σ_0	Reference stress	10 MPa	[7]
K	Permeability	$7.77 \cdot 10^{-18}$ m^2	[7,21]
ϕ_0	Initial porosity	0.21	[21,22]
κ^{F}	Fluid bulk modulus	3.95 GPa	[7,23]
ρ^{F}_0	Initial fluid density	1.35 g/cm^3	[24]

where $\alpha^{\mathrm{ch}}_{\mathrm{L}}$ and $\alpha^{\mathrm{ch}}_{\mathrm{T}}$ are the longitudinal and transverse chemical expansion coefficients of the fibre, respectively. The resulting 2nd Piola–Kirchhoff stress $\boldsymbol{S}$ is derived from a St-Venant hyperelastic potential ψ defined on the intermediate configuration as

$$\boldsymbol{S} = \mathsf{L}(c_{\mathrm{Li}}) : \left[\boldsymbol{E} - \boldsymbol{E}^{\mathrm{ch}}(c_{\mathrm{Li}})\right], \tag{18}$$

where $\mathsf{L}(c_{\mathrm{Li}})$ is the concentration-dependent transversely isotropic stiffness tensor, defined from the material properties for carbon fibres in Table 1. Furthermore, $\boldsymbol{E} = \frac{1}{2}[\boldsymbol{F}^{\mathrm{T}} \cdot \boldsymbol{F} - \boldsymbol{I}]$ and $\boldsymbol{E}^{\mathrm{ch}}(c_{\mathrm{Li}}) = \frac{1}{2}[[\boldsymbol{F}^{\mathrm{ch}}(c_{\mathrm{Li}})]^{\mathrm{T}} \cdot \boldsymbol{F}^{\mathrm{ch}}(c_{\mathrm{Li}}) - \boldsymbol{I}]$ are the total and chemical Green–Lagrange strains, respectively.

4.2. Description of the SBE matrix domain

The SBE domain Ω^{SBE} is treated as a deforming porous medium where the solid skeleton exhibits a visco-hyperelastic response. To capture the rate-dependent behaviour of the polymer, we adopt a finite deformation Zener model (three-parameter model) via a multiplicative split of the skeleton deformation gradient into elastic and viscous parts, $\boldsymbol{F} = \boldsymbol{F}^{\mathrm{e}} \cdot \boldsymbol{F}^{\mathrm{v}}$. The mechanical response of both the equilibrium and non-equilibrium branches are characterized by Neo-Hookean free energy functionals. For the equilibrium branch, the energy ψ^{EQ} is a function of the total right Cauchy–Green tensor $\boldsymbol{C}$ scaled by the static shear and bulk moduli given in Table 1. The energy associated with the non-equilibrium branch, ψ^{NEQ}, is defined in terms of the elastic part $\boldsymbol{C}^{\mathrm{e}} = [\boldsymbol{F}^{\mathrm{v}}]^{-\mathrm{T}} \cdot \boldsymbol{C} \cdot [\boldsymbol{F}^{\mathrm{v}}]^{-1}$ and involves the dynamic shear modulus, relaxation time, norton exponent and reference stress values in Table 1. The dissipative behaviour is then introduced via a Norton-type evolution law for the viscous deformation $\boldsymbol{F}^{\mathrm{v}}$. Furthermore, the total 2nd Piola–Kirchhoff stress $\boldsymbol{S}$ is decomposed into the effective stress contribution from the solid skeleton, $\boldsymbol{S}'$, and the contribution from the pore pressure p

$$\boldsymbol{S} = \boldsymbol{S}' - J p \boldsymbol{C}^{-1}, \tag{19}$$

where $\boldsymbol{S}'$ is derived from the equilibrium and non-equilibrium potentials mentioned above. The total 1st Piola–Kirchhoff stress $\boldsymbol{P}$, which is the equilibrium stress, is subsequently defined as $\boldsymbol{P} = \boldsymbol{F} \cdot \boldsymbol{S} = \boldsymbol{P}' - J p \boldsymbol{F}^{-\mathrm{T}}$. The total Cauchy stress $\boldsymbol{\sigma}$ is expressed as

$$\boldsymbol{\sigma} = \frac{1}{J} \boldsymbol{P} \cdot \boldsymbol{F}^{\mathrm{T}} = \boldsymbol{\sigma}' - p\boldsymbol{I}, \tag{20}$$

where $\boldsymbol{\sigma}'$ represents the effective Cauchy stress in the solid skeleton.

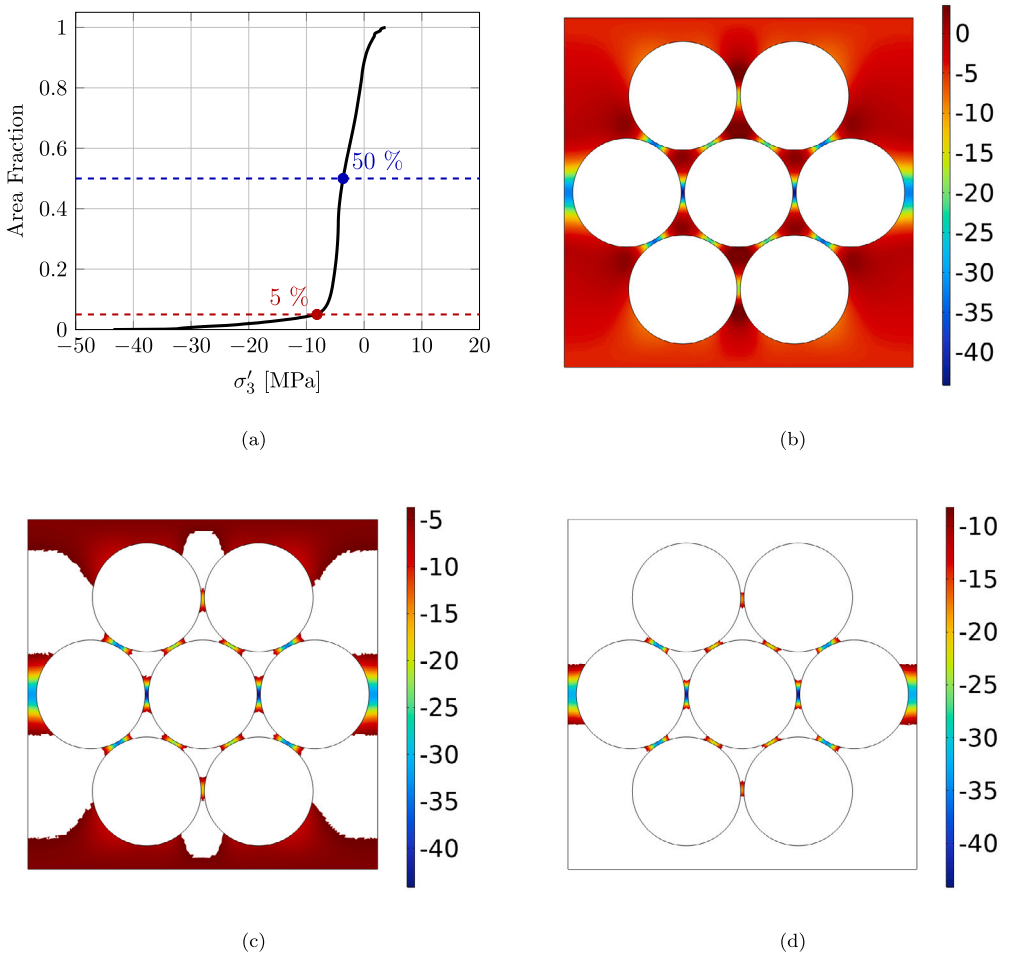

Fig. 2. Hexagonal reference model analysis at full lithiation ($c_{\mathrm{Li}} = 1$): (a) Area-weighted cumulative distribution function (CDF) of the minimum effective principal stress, σ_3', with markers indicating the median (50%) and tail (5%) thresholds. Spatial distribution of σ_3' [MPa] shown for: (b) the full matrix domain with 100% area fraction. (c) 50% area fraction. (d) 5% area fraction.

Moreover, the solid phase is assumed locally incompressible ($\rho^{\mathrm{s}} =$ const.), the macroscopic SBE domain is compressible due to the evacuation or accumulation of the liquid electrolyte within the pores. The current porosity ϕ evolves with the total volume ratio $J = \det(\boldsymbol{F})$ as

$$\phi(J) = 1 - \frac{1}{J}[1 - \phi_0]. \tag{21}$$

The transport of the liquid electrolyte through the porous skeleton is driven by the pore pressure gradient $\boldsymbol{\nabla}_X p$, following Darcy's law in the reference configuration

$$\phi \boldsymbol{W} = -K \boldsymbol{I} \cdot \boldsymbol{\nabla}_X p, \tag{22}$$

where K is the isotropic permeability. The fluid itself is assumed to be compressible, with a density $\rho^{\mathrm{F}}(p)$ governed by the intrinsic bulk modulus κ^{F}.

5. Results

5.1. Properties of the structural negative electrode

The geometric characteristics and measured fibre volume fractions of the ten SEM micrographs are summarized in Table 2. Furthermore, all SEM micrographs are provided in Figure S1–S10, in the supplementary information. While the image width remains highly consistent at approximately 89 μm, the domain height and local fibre density exhibit significant stochastic variation—a characteristic of the manufacturing-induced heterogeneity in structural battery composites. The measured fibre volume fraction μ ranges from 0.429 to 0.599, reflecting local fluctuations in the packing density. To ensure the reconstructed RVEs represent the global state of the laminate, the ensemble average of $\mu \approx 0.531$ is adopted as the target volume fraction for both the stochastic reconstructions and the hexagonal reference model.

Table 2
Geometric properties and measured fibre volume fractions for the ten SEM micrographs used for spatial statistics extraction and RVE reconstruction.

Image index	Width [μm]	Height [μm]	Fibre Vol. Fraction
1	88.88	20.84	0.590
2	88.88	27.63	0.599
3	88.82	19.99	0.588
4	88.93	22.39	0.569
5	88.93	25.23	0.501
6	88.93	27.79	0.464
7	88.93	31.80	0.429
8	88.99	22.98	0.501
9	88.88	24.32	0.512
10	88.99	25.28	0.561
Mean	**88.92**	**24.83**	**0.531**
Std. Dev.	0.054	3.51	0.059

5.2. Reference model

To establish a baseline for the numerical stress analysis, a deterministic reference model is generated using a perfectly ordered hexagonal

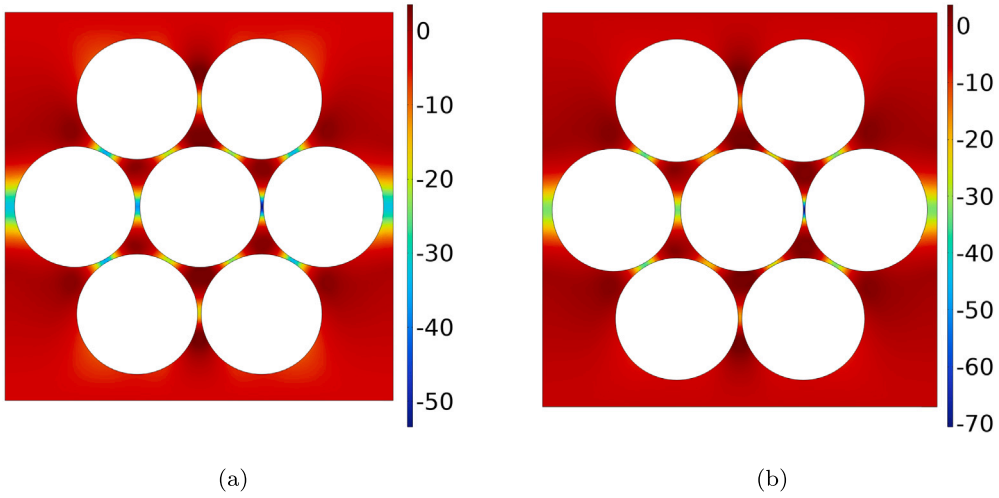

Fig. 3. Modified hexagonal reference model analysis at full lithiation ($c_{Li} = 1$): (a) Minimum effective principal stress, σ_3' [MPa], in the SBE matrix for an offset central fiber resulting in a local clearance of $h = 0.1125$ μm. (b) Minimum effective principal stress, σ_3' [MPa], for a local clearance of $h = 0.075$ μm.

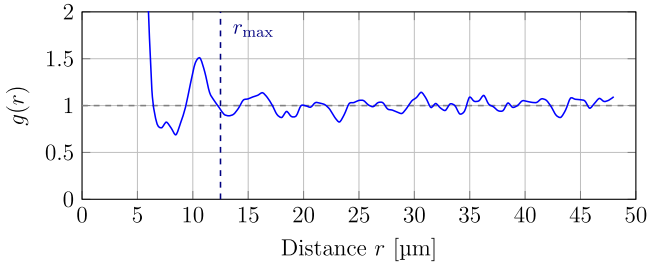

Fig. 4. Pair correlation function $g(r)$ in Eq. (6). The convergence to $g(r) \approx 1$ at $r_{max} = 12.5$ μm.

arrangement of seven fibres. This model represents a uniform fibre distribution with a constant fibre volume fraction $\mu = 0.531$, a fibre diameter of 5 μm and a fixed nearest-neighbour clearance of $h = 0.15$ μm. A uniform cross-sectional diameter of 5 μm is assumed for all carbon fibres to isolate the sensitivity in stresses in the matrix with respect to centroid-driven spatial clustering. In reality, however, carbon fibres exhibit minor diameter fluctuations. Introducing variation in the fibre diameter would impose an additional stochastic variable in the reconstruction and reference, likely altering the largest stress magnitudes in the matrix reported herein.

The resulting area-weighted cumulative distribution function (CDF) for the minimum effective principal stress, σ_3', at full lithiation ($c_{Li} = 1$) is shown in Fig. 2a, with markers highlighting the median (50%) and extreme (5%) stress thresholds. Note that the effective stress is the stress in the solid polymer skeleton of the SBE as defined in Eq. (20). The corresponding spatial stress distributions are illustrated in Fig. 2b–d. It should be noted that the adoption of a multiaxial failure criterion is outside the scope of this study, as experimental data to calibrate such failure envelopes for this specific SBE material are currently unavailable. The primary focus is placed on the minimum effective principal stress where localized compressive crushing is expected to be the dominant mechanical degradation mode during lithiation.

In Fig. 2b, the minimum effective principal stresses in the full matrix domain (100% area fraction), are shown. The peak compressive stresses are observed to be localized within the narrow matrix ligaments between adjacent fibres, where mechanical confinement is most severe. Conversely, stress magnitudes relax significantly in the larger regions between fibre triplets. By applying area-fraction thresholds to the domain, the transition from the bulk response to the localized peak is visualized. While the median stress distribution at 50% area fraction characterizes the broader matrix response in Fig. 2c, the 5% threshold isolates the most critical regions where compressive stresses exceed −8 MPa shown in Fig. 2d. This reference model serves as a benchmark to evaluate the impact of nonuniform fibre arrangements in reconstructed RVEs.

The mechanical importance of the localized peaks in compressive stress is emphasized by recent observations by Pipertzis et al. [25], who reported an increase in effective ionic conductivity over the structural negative electrode after lithiation-delithiation cycles. This suggests that the electrolyte undergoes structural degradation, likely driven by the localized crushing of the SBE as it accommodates fibre expansion. Although this specific damage mechanism remains to be definitively confirmed, the potential formation of additional ionic pathways highlights the necessity of investigating the SBE's response under high-confinement compressive states. Consequently, this hexagonal reference model serves as a benchmark to evaluate how nonuniform fibre arrangements and the resulting stochastic amplification of stresses further impact the structural integrity of the electrolyte.

5.3. Sensitivity to local inter-fibre spacing

To isolate the physical sensitivity of the localized compressive fields to the nearest-neighbour distance, we conduct a parametric study on the reference model by introducing a controlled geometric nonuniformity. In the baseline hexagonal configuration in Section 5.2, the nearest-neighbour clearance parameter h is uniformly restricted to 0.15 μm. Here, we systematically perturb this arrangement by displacing the central fibre horizontally towards the right, reducing the localized clearance to $h = 0.1125$ μm and $h = 0.075$ μm while maintaining the global periodic boundaries intact.

Fig. 3 shows the resulting minimum effective principal stress field in the SBE matrix at full lithiation ($c_{Li} = 1$). When the clearance is reduced to $h = 0.1125$ μm in Fig. 3a, the most localized compressive stress increases from approximately −40 MPa in the uniform reference case to −50 MPa. This amplification effect becomes increasingly nonlinear as the nearest-neighbour clearance narrows; for $h = 0.075$ μm in Fig. 3b, the peak localized compression increases to approximately −70 MPa. It must be emphasized, however, that as we decrease the inter-fibre clearance, the underlying assumptions of classical local continuum mechanics becomes less justified and the model for the SBE becomes less accurate. Therefore, rather than reading these high stress numbers as exact physical realities, they should be interpreted as a flag that local material uniformity is potentially lost in such narrow gaps.

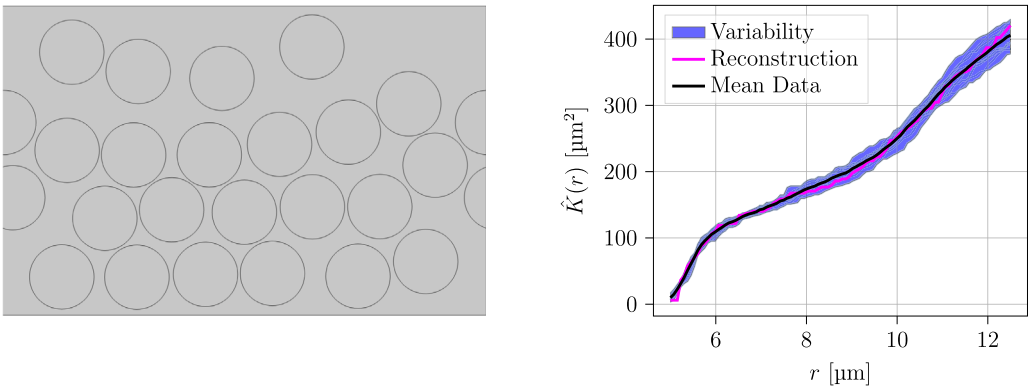

Fig. 5. Validation of the RVE reconstruction: (a) Representative generated geometry showing the final fibre centroid positions for $W = 37.5$ µm. (b) Comparison of the estimated Ripley's K-function for the reconstructed RVE against the experimental mean and the variability band (shaded area) established from ten SEM images.

5.4. Validation of RVE reconstruction

The first step in the reconstruction process is to identify the spatial range over which fibre centroids exhibit significant correlation. Fig. 4 presents the pair correlation function in Eq. (6), averaged across the ten SEM images. The results show a clear exclusion zone for $r < 5$ µm , followed by a primary peak at $r \approx 10.6$ µm, indicating a structural preference for specific fibre spacings within the electrode cross-section. The pair correlation function $g(r)$ converges to unity at approximately 12.5 µm, marking the distance at which the fibre arrangement becomes completely spatially random. This distance effectively defines the correlation length of the microstructure; consequently, $r_{\max} = 12.5$ µm is established as the evaluation radius for all subsequent RVE reconstructions.

The spatial fidelity of the fibre distribution is now evaluated to ensure the generated microstructure accurately represents the physical specimens. A successful reconstruction of the fibre distribution is shown in Fig. 5a, where the centroids have been positioned according to the prescribed spatial constraints. To verify the accuracy of the RVE generation algorithm, the Ripley's K-function of the reconstructed centroids was evaluated against the experimental targets established in Section 3.5. As specified in the convergence criterion of Algorithm 1, the reconstruction is accepted once the simulated K-function falls within the experimental variability band. As shown in Fig. 5b, the final reconstructed curve closely follows the target mean $\langle \hat{\boldsymbol{K}}_{\text{observed}} \rangle$ and remains consistent within the experimental limits. The agreement confirms that the stochastic optimization successfully preserve the second-order spatial properties of reconstructed fibres, resulting in a statistically representative volume element.

With the representative nature of the reconstructions established, these geometries serve as the basis for evaluating the impact of microstructural variability on local mechanical integrity. For each considered RVE width W, we generate five independent RVE realizations to capture the inherent variability of the fibre arrangement. Each realization is subjected to the boundary value problem specifics outlined in Section 4.

5.5. Compressive stresses in the SBE

The resulting area weighted CDFs of the minimum effective principal stress, σ_3', recorded within the SBE matrix at full lithiation is presented in Fig. 6 for five unique RVE widths. Fig. 6a represents the smallest width $W = 18.75$ µm. There is a significant dispersion between the five stochastic realizations which emerges around −15 MPa, corresponding to approximately 5% area fraction. As the RVE width increases from $W = 37.5$ µm in Fig. 6b to $W = 112.5$ µm in Fig. 6e, the variance formed by the blue curves narrows significantly at $\sigma_3' = -15$ MPa. For the largest width in Fig. 6e, the realizations nearly collapse onto a single master curve, suggesting that the volume is large enough to average out local stochastic variations in fibre placement. Notably, in all subfigures, the stochastic RVEs consistently exhibit more severe variance in the tail regions (leftmost side of the plots). While the stresses around 10% area fraction of the stochastic models eventually stabilizes near the hexagonal benchmark, the peak compressive stresses corresponding to the 0.1% area fraction is significantly higher than those predicted by the reference model. The discrepancy in these localized regions indicates an amplified stress state due to nonuniformity in the microstructure, where random fibre proximity in the stochastic models creates higher local confinement than the perfectly spaced hexagonal arrangement.

To further determine the RVE size for the SBE microstructure, the convergence of the minimum effective principal stress, σ_3', is analysed as a function of the RVE width. Fig. 7 summarizes the mean and standard deviation for four area fraction thresholds; the median response at 50%, and the tails at 5%, 1%, and 0.25%. The median stress demonstrates stabilizing near the deterministic hexagonal benchmark of −3.65 MPa even at the smallest considered RVE width. The standard deviation at this threshold is negligible, resulting in error bars that are nearly invisible at the current scale. This indicates that the bulk matrix environment is statistically homogeneous and insensitive to local stochastic fibre arrangements.

In contrast to the median response, the 5% area fraction thresholds exhibit a significant deviation from the deterministic hexagonal benchmark. While the stochastic mean values stabilize as the RVE width increases, they converge towards a more compressive stress value than the reference model. The stochastic RVEs settle near −10.3 MPa, exceeding in absolute value the −8.18 MPa predicted by the reference model. The nonuniformity in the fibre arrangement causes localized confinement zones and stress concentrations that are absent in periodic arrangements. However, as the area fraction is further decreased to 1%, we see that the relationship between the stochastic and deterministic models shift. While the hexagonal model predicts a 1% area fraction stress of −27.77 MPa, the stochastic RVEs converge to a less compressive value of approximately −21.7 MPa. The perfectly ordered hexagonal

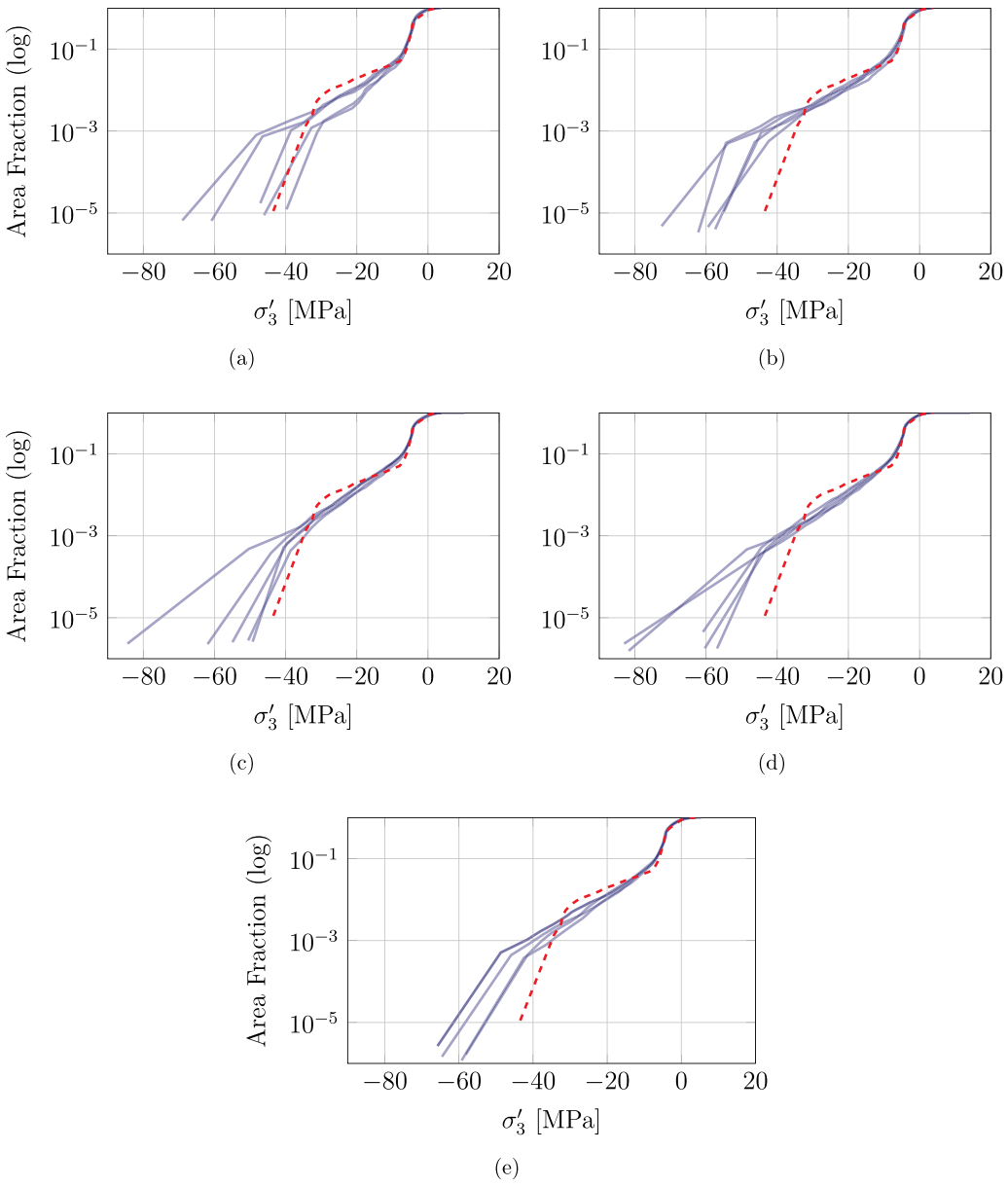

Fig. 6. Cumulative distribution functions of minimum effective principal stress in the matrix σ_3', evaluated at $c_{\mathrm{Li}} = 1$ for different RVE widths: (a) $W = 18.75$ μm, (b) $W = 37.5$ μm, (c) $W = 62.5$ μm, (d) $W = 87.5$ μm, and (e) $W = 112.5$ μm. Blue curves represent five individual stochastic realizations per considered width, while the red dashed line indicates the deterministic hexagonal reference model.

arrangement imposes a higher degree of confinement over a larger area of the matrix. Finally, at the 0.25% threshold, the stochastic means converge almost exactly to the hexagonal benchmark of −32.6 MPa. For extremely local stresses corresponding to area fractions lower than 10^{-3} in Fig. 6, we see that the stochastic models produce lower stress magnitudes compared to the uniform hexagonal reference model for all widths considered. Furthermore, the minimum observed stresses are accompanied by high variance.

The associated standard deviation in Fig. 7 generally goes down as the RVE width increases, indicative that the matrix response becomes less sensitive to local stochastic fluctuations as RVE width increases. The highest stress magnitudes at 0.25% area fraction also demonstrate the greatest sensitivity to the RVE size. For small widths $W = 18.75$ μm, the large standard deviation (≈3.48 MPa) reflects the high probability of either capturing or missing a critical near-contact events within a limited volume. As the width increases to $W = 112.5$ μm, the mean stress stabilizes and the standard deviation narrows significantly to 2.05 MPa. The decrease in standard deviation suggest that the larger RVEs contains sufficiently many of the critical clustering sites to be considered statistically representative.

6. Discussion

The convergence analysis presented in Fig. 7 highlights that the definition of a representative volume of the structural negative electrode is not a fixed geometric constant but is instead dependent on the mechanical metric of interest. While a small RVE width of $W = 18.75$ μm is sufficient to characterize the bulk median stress response at 50% area fraction, it fails to provide a stable estimate for the extreme compressive stress tails that likely govern structural integrity.

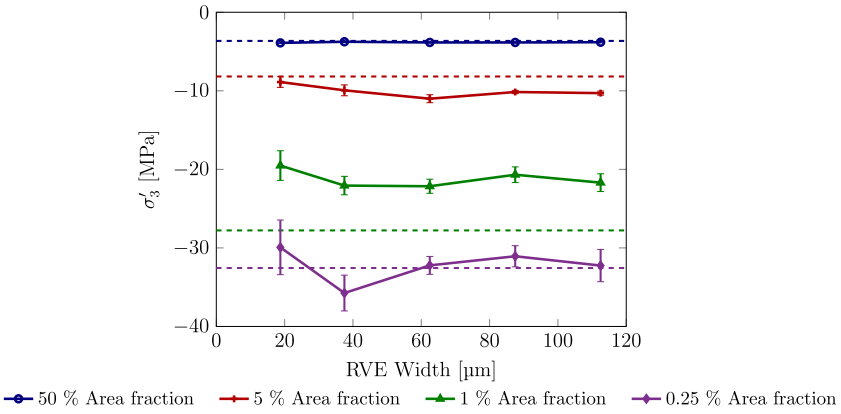

Fig. 7. Convergence of the minimum effective principal stress σ_3' as a function of RVE width W. Solid lines and markers represent the mean stochastic response across five realizations, with error bars indicating the standard deviation. Dashed lines of corresponding colours denote the deterministic hexagonal reference for each area fraction threshold.

For the SBE system, an RVE width of $W = 62.5$ µm appears to offer a pragmatic balance; the standard deviations for the 5% and 1% thresholds have significantly tightened, providing a statistically reliable estimate of stresses induced by nonuniformity. However, interpreting these localized stress peaks in the context of material failure remains a significant challenge. Current understanding of SBE yield behaviour is largely limited to bulk uniaxial compression and tension measurements reported by Tavano et al. [26]. The direct translation of such macro-scale fracture to the microscopic ligaments between fibres, where the clearance is as small as 0.15 µm is questionable as the dimensions of the pore structure are at the same scale. At these sub-micron scales, where pore sizes range from approximately 10 to 100 nm, size effects introduce significant uncertainty regarding material behaviour. Consequently, it cannot be assumed that the strength measured for the bulk SBE translates directly to the local inter-fibre scale, where the failure mechanics may be governed by different characteristic length scales.

The discrepancies identified in this study highlight that a nonuniform microstructure is essential to accurately predict local stress states within the SBE matrix. While the hexagonal reference model provides a useful baseline, it cannot account for the stochastic amplification of stresses caused by fibre clustering. The hexagonal model is not always safer or more conservative. At the 1% area fraction, the perfect hexagonal grid predicts compressive stresses higher than random RVEs, since it assumes that every fibre is equally cramped. In reality, a random arrangement has both tight clusters and relief zones where fibres are further apart. This shows that a uniform hexagonal model is too simplistic to resolve the full spectrum of compressive intensities.

Relying on Ripley's K-function alone as the primary optimization target introduces an inherent limitation, as this second-order global descriptor can average out local features such as the nearest-neighbour distance distribution. In this work, the microstructural risk associated with the global averaging are mitigated by two key features of the modelling workflow. Firstly, the reconstruction algorithm enforces a non-overlap and minimum fibre-to-fibre clearance constraint, $d_{\min} = 2r_f + h$, which serves as a first-order descriptor bounding the minimum possible SBE ligament thickness. The constraint further prevents fibre-to-fibre contact that could generate artificial stress singularities. Secondly, instead of relying on a single optimized RVE, five independent stochastic configurations are simulated per domain width. By sampling different local fibre arrangement variations that all satisfy the global experimental K-function band, the statistical distribution and tails (e.g., the 1 % and 5 % area fractions) of the compressive stress field are captured. Nevertheless, incorporating additional multi-descriptor objectives, such as the probability density function of nearest neighbours directly into the optimization loss function, represents a step to further tighten the local fidelity in future microstructural reconstructions.

7. Conclusions and outlook

This study establishes a geometric and statistical proposal for RVE reconstruction based on SEM images of a structural negative electrode, focusing on the localized compressive stresses in the structural battery electrolyte induced by carbon fibre expansion. We conclude that the definition of a representative volume is dependent on the mechanical metric of interest; while a small RVE width of $W = 18.75$ µm is sufficient to characterize the bulk median stress response, a width of $W = 62.5$ µm is in general, deemed sufficient to achieve stable and representative estimates of the stress tails. A nonuniform microstructure is essential for these predictions, as idealized hexagonal models fail to resolve the full spectrum of compressive stresses. Specifically, stochastic arrangements capture both the amplified stress zones within fibre clusters and the corresponding relief zones in open gaps. By identifying this stochastic amplification, we showed that a uniform hexagonal microstructure models can be non-conservative, underestimating the localized confinement by approximately 25% at the 5% area fraction threshold.

As to future work, the mechanical interpretation of these localized stress peaks remains a critical open question. Future research can prioritize nano-scale characterization to determine the local yield stresses or strength properties of the SBE matrix within sub-micron gaps. Additionally, incorporating damage modelling into these RVE simulations will be vital to evaluate if localized clusters evolve into micro cracks.

CRediT authorship contribution statement

Carl Larsson: Writing – review & editing, Writing – original draft, Visualization, Validation, Methodology, Investigation, Formal analysis, Data curation, Conceptualization. **Ramesh Talreja:** Writing – review & editing, Writing – original draft, Supervision, Methodology, Conceptualization. **Fredrik Larsson:** Writing – review & editing, Writing – original draft, Supervision, Methodology, Formal analysis, Conceptualization. **Richa Chaudhary:** Writing – review & editing, Methodology, Data curation, Conceptualization. **Amanda Persdotter:** Writing – review & editing, Methodology, Data curation. **Leif E. Asp:** Writing – review & editing, Writing – original draft, Supervision, Resources, Project administration, Methodology, Investigation, Funding acquisition, Conceptualization.

Declaration of competing interest

The authors declare that they have no known competing financial interests or personal relationships that could have appeared to influence the work reported in this paper.

Acknowledgements

The project is funded by the USAF via the EOARD Award No. FA8655-25-1-7049, ONR, USA, Award No. N62909-22-1-2037, Swedish Research Council, grant number 2020-05057, and 2D TECH VINNOVA competence Center, grant number 2019-00068. Also, Barbro Oshers Pro Suecia Foundation is greatly acknowledged.

Appendix A. Supplementary data

Supplementary material related to this article can be found online at https://doi.org/10.1016/j.compscitech.2026.111760.

Data availability

Data will be made available on request.

References

[1] L.E. Asp, K. Bouton, D. Carlstedt, S. Duan, R. Harnden, W. Johannisson, M. Johansen, M.K. Johansson, G. Lindbergh, F. Liu, et al., A structural battery and its multifunctional performance, Adv. Energy Sustain. Res. 2 (3) (2021) 2000093.

[2] R. Chaudhary, J. Xu, Z. Xia, L.E. Asp, Unveiling the multifunctional carbon fiber structural battery (adv. mater. 48/2024), Adv. Mater. 36 (48) (2024) 2470382, http://dx.doi.org/10.1002/adma.202470382.

[3] E.S. Greenhalgh, S. Nguyen, L.E. Asp, A. Bici, A. Bismarck, D. Fam, M. Johansson, G. Lindbergh, J.L. Lutkenhaus, M.S.P. Shaffer, N. Shirshova, M. Srinivasan, J. Xu, D. Zenkert, Characterization and reporting protocols for structural power composites: A perspective, Adv. Energy Mater. 15 (42) (2025) e04702, http://dx.doi.org/10.1002/aenm.202404702, arXiv:https://advanced.onlinelibrary.wiley.com/doi/pdf/10.1002/aenm.202404702 URL https://advanced.onlinelibrary.wiley.com/doi/abs/10.1002/aenm.202404702.

[4] G. Lim, K. Chan, N. Sutrisnoh, M. Srinivasan, Design of structural batteries: carbon fibers and alternative form factors, Mater. Today Sustain. 20 (2022) 100252, http://dx.doi.org/10.1016/j.mtsust.2022.100252, URL https://www.sciencedirect.com/science/article/pii/S2589234722001440.

[5] K. Bouton, L. Schneider, D. Zenkert, G. Lindbergh, A structural battery with carbon fibre electrodes balancing multifunctional performance, Compos. Sci. Technol. 256 (2024) 110728, http://dx.doi.org/10.1016/j.compscitech.2024.110728, URL https://www.sciencedirect.com/science/article/pii/S0266353824002987.

[6] M.S. Siraj, S. Tasneem, D. Carlstedt, S. Duan, M. Johansen, C. Larsson, J. Xu, F. Liu, F. Edgren, L.E. Asp, Advancing structural battery composites: robust manufacturing for enhanced and consistent multifunctional performance, Adv. Energy Sustain. Res. 4 (11) (2023) 2300109.

[7] C. Larsson, F. Larsson, R. Tavano, J. Xu, K. Runesson, L.E. Asp, Poro-mechanical analysis of a structural battery electrolyte: Experimental study and model calibration, Mech. Mater. 216 (2026) 105632, http://dx.doi.org/10.1016/j.mechmat.2026.105632, URL https://www.sciencedirect.com/science/article/pii/S0167663626000360.

[8] C. Larsson, F. Larsson, J. Xu, K. Runesson, L.E. Asp, Effects of lithium insertion induced swelling of a structural battery negative electrode, Compos. Sci. Technol. 244 (2023) 110299, http://dx.doi.org/10.1016/j.compscitech.2023.110299.

[9] R. Hill, Elastic properties of reinforced solids: Some theoretical principles, J. Mech. Phys. Solids 11 (5) (1963) 357–372, http://dx.doi.org/10.1016/0022-5096(63)90036-X, URL https://www.sciencedirect.com/science/article/pii/002250966390036X.

[10] R. Pyrz, Correlation of microstructure variability and local stress field in two-phase materials, Mater. Sci. Eng.: A 177 (1) (1994) 253–259, http://dx.doi.org/10.1016/0921-5093(94)90497-9, URL https://www.sciencedirect.com/science/article/pii/0921509394904979.

[11] B.D. Ripley, Modelling spatial patterns, J. R. Stat. Soc. Ser. B Stat. Methodol. 39 (2) (1977) 172–192, http://dx.doi.org/10.1111/j.2517-6161.1977.tb01615.x, arXiv:https://rss.onlinelibrary.wiley.com/doi/pdf/10.1111/j.2517-6161.1977.tb01615.x URL https://rss.onlinelibrary.wiley.com/doi/abs/10.1111/j.2517-6161.1977.tb01615.x.

[12] D. Trias, J. Costa, A. Turon, J. Hurtado, Determination of the critical size of a statistical representative volume element (SRVE) for carbon reinforced polymers, Acta Mater. 54 (13) (2006) 3471–3484, http://dx.doi.org/10.1016/j.actamat.2006.03.042, URL https://www.sciencedirect.com/science/article/pii/S1359645406002497, Selected Papers from the Meeting "Micromechanics and Microstructure Evolution: Modeling, Simulation and Experiments" held in Madrid/Spain, 11–16 September 2005.

[13] Y. Ding, P. Camanho, A. Silva, Micromechanical modelling of unidirectional continuous fibre-reinforced composites: A review, Compos. B 309 (2026) 113036, http://dx.doi.org/10.1016/j.compositesb.2025.113036, URL https://www.sciencedirect.com/science/article/pii/S1359836825009473.

[14] S.A. Elnekhaily, R. Talreja, Damage initiation in unidirectional fiber composites with different degrees of nonuniform fiber distribution, Compos. Sci. Technol. 155 (2018) 22–32, http://dx.doi.org/10.1016/j.compscitech.2017.11.017, URL https://www.sciencedirect.com/science/article/pii/S0266353817308898.

[15] F. Goreaud, R. Pélissier, On explicit formulas of edge effect correction for Ripley's K-Function, J. Veg. Sci. 10 (3) (1999) 433–438, URL http://www.jstor.org/stable/3237072.

[16] A.A. Gusev, P.J. Hine, I.M. Ward, Fiber packing and elastic properties of a transversely random unidirectional glass/epoxy composite, Compos. Sci. Technol. 60 (4) (2000) 535–541.

[17] S. Kirkpatrick, C.D. Gelatt, M.P. Vecchi, Optimization by simulated annealing, Science 220 (4598) (1983) 671–680.

[18] N. Metropolis, A.W. Rosenbluth, M.N. Rosenbluth, A.H. Teller, E. Teller, Equation of state calculations by fast computing machines, J. Chem. Phys. 21 (6) (1953) 1087–1092.

[19] S. Duan, A.H. Iyer, D. Carlstedt, F. Rittweger, A. Sharits, C. Maddox, K.-R. Riemschneider, D. Mollenhauer, M. Colliander, F. Liu, L.E. Asp, Effect of lithiation on the elastic moduli of carbon fibres, Carbon 185 (2021) 234–241, http://dx.doi.org/10.1016/j.carbon.2021.09.037.

[20] D. Carlstedt, F. Rittweger, K. Runesson, A.M. Navarro-Suarez, J. Xu, S. Duan, F. Larsson, K.-R. Riemschneider, L.E. Asp, Experimental and computational characterization of carbon fibre based structural battery electrode laminae, Compos. Sci. Technol. 220 (2022) 109283.

[21] D. Carlstedt, K. Runesson, F. Larsson, V. Tu, R. Jänicke, L.E. Asp, Computational modelling of structural batteries accounting for stress-assisted convection in the electrolyte, Int. J. Solids Struct. 238 (2022) 111343, http://dx.doi.org/10.1016/j.ijsolstr.2021.111343.

[22] S. Duan, M. Cattaruzza, V. Tu, R.M. Auenhammer, R. Jänicke, M.K.G. Johansson, F. Liu, L.E. Asp, Three-dimensional reconstruction and computational analysis of a structural battery composite electrolyte, Commun. Mater. 4 (2023) 49, http://dx.doi.org/10.1038/s43246-023-00377-0.

[23] A.A. Wang, D. Persa, S. Helin, K.P. Smith, J.L. Raymond, C.W. Monroe, Compressibility of lithium hexafluorophosphate solutions in two carbonate solvents, J. Chem. Eng. Data 68 (4) (2023) 805–812, http://dx.doi.org/10.1021/acs.jced.2c00711.

[24] Canrud, 2025, URL https://www.canrud.com/products/detail/2840. (Accessed 14 October 2025).

[25] A. Pipertzis, J. Xu, N. Abdou, A. Martinelli, L. Asp, J. Swenson, Ionic and electronic conductivity in structural negative electrodes, Electrochim. Acta 512 (2025) 145501, http://dx.doi.org/10.1016/j.electacta.2024.145501.

[26] R. Tavano, M. Spagnol, N. Al-Ramahi, R. Joffe, J. Xu, L.E. Asp, Mechanical characterisation of a structural battery electrolyte, Polymer 312 (2024) 127646, http://dx.doi.org/10.1016/j.polymer.2024.127646.